VoxHenry: FFT-Accelerated Inductance Extraction for Voxelized Geometries

Abdulkadir C. Yucel, Ioannis P. Georgakis, Athanasios G. Polimeridis, *Senior Member, IEEE*, Hakan Bağcı, *Senior Member, IEEE*, and Jacob K. White, *Fellow, IEEE*

***Abstract*— VoxHenry, a fast Fourier transform (FFT)-accelerated integral-equation-based simulator for extracting frequency-dependent inductances and resistances of structures discretized by voxels, is presented. VoxHenry shares many features with the popular inductance extractor, FastHenry. Just like FastHenry, VoxHenry solves a combination of the electric volume integral equation and the current continuity equation, but with three distinctions that make VoxHenry suitable and extremely efficient for analyzing voxelized geometries: 1) it leverages a carefully selected set of piecewise-constant and piecewise-linear basis functions; 2) it exploits FFTs to accelerate the matrix–vector multiplications during the iterative solution of system of equations; and 3) it employs a sparse preconditioner to ensure the rapid convergence of iterative solution. VoxHenry is capable of accurately computing frequency-dependent inductances and resistances of arbitrarily shaped and large-scale structures on a desktop computer. The accuracy, efficiency, and applicability of VoxHenry are demonstrated through inductance analysis of various structures, including square and circular coils as well as arrays of RF inductors (situated over ground planes).**

***Index Terms*— Fast Fourier transform (FFT), FastHenry, inductance extraction, magneto-quasistatic analysis, parasitic extraction, partial element equivalent circuit, volume integral equation (VIE), voxelized geometries.**

I. Introduction

With ever increasing operating frequencies and shrinking electronic device sizes, postlayout parasitic extraction tools became indispensable for almost every digital design explorations. Today, these tools are commonly used not only for assessing functional verification and timing loop closure but also for estimating power and checking electrical fault (e.g., IR drop) [1]. Modern parasitic extractors are fast enough for being used in iterative digital design exploration and sufficiently accurate for being employed in some analog design flows. Nevertheless, these extractors were not developed for handling high-performance mixed signal-integrated circuits, including high-accuracy analog-to-digital converters and (near-) terahertz circuits [2]. To address the needs of mixed signal designers, extractors were improved to handle complex 3-D geometries and extract dense coupling due to longer-range inductive effects. However, the enhanced extractors are not suitable to be conveniently used in rapid iterative exploration of mixed signal designs.

Recent advances in computer graphics have ushered in a new breed of process emulation tools that are fast and accurate enough to be used in high-performance mixed signal design flows. These tools leverage voxel-based representations for visualization during unit process steps, exploit the simplicity of manipulating voxels (i.e., cubes) for automatically, quickly, and accurately generating 3-D structures from process descriptions/layouts, and allow representing the geometries with billions of voxels. Fortunately, such representations of structures/geometries with voxels (i.e., voxelized structures/geometries) are perfectly suitable for fast Fourier transform (FFT)-accelerated volume integral equation (VIE) simulators [3]–[8]. Nevertheless, no parasitic inductance extractor for voxelized structures has been proposed so far.

In this paper, VoxHenry, an FFT-accelerated inductance extractor for voxelized geometries, is presented. VoxHenry shares many features with the popular FastHenry inductance extractor [9]. Just like FastHenry, VoxHenry solves a combination of electric field VIE and current conservation equation simultaneously, but with three main distinctions as follows.

1) VoxHenry uses a carefully selected set of divergence-free basis functions consisting of three piecewise-constant and two piecewise-linear basis functions to represent the current in every voxel and to preserve current continuity around the corners.
2) VoxHenry exploits FFTs to perform fast matrix vector multiplications (MVMs) during the iterative solution linear system of equations arising upon discretization of the volume integral and current conservation equations.
3) VoxHenry leverages a sparse preconditioner to achieve rapid convergence while iteratively solving the linear system of equations.

VoxHenry is capable of efficiently and accurately extracting inductances of large-scale and arbitrarily shaped structures on a desktop computer. The capability, accuracy, and efficiency of the VoxHenry simulator are demonstrated through

Manuscript received July 18, 2017; revised October 9, 2017 and November 30, 2017; accepted December 12, 2017. Date of publication January 18, 2018; date of current version April 3, 2018. This work was supported in part by a grant from Skoltech as part of the Skoltech-MIT Next Generation Program. *(Corresponding author: Abdulkadir C. Yucel.)*

A. C. Yucel is with the Department of Electrical Engineering and Computer Science, Massachusetts Institute of Technology, Cambridge, MA 02139 USA, and also with the Division of Computer, Electrical, and Mathematical Science and Engineering, King Abdullah University of Science and Technology, Thuwal 23955-6900, Saudi Arabia (e-mail: acyucel@mit.edu).

I. P. Georgakis and A. G. Polimeridis are with the Center for Computational Data-Intensive Science and Engineering, Skolkovo Institute of Science and Technology, Moscow 143026, Russia.

H. Bağcı is with the Division of Computer, Electrical, and Mathematical Science and Engineering, King Abdullah University of Science and Technology, Thuwal 23955-6900, Saudi Arabia.

J. K. White is with the Department of Electrical Engineering and Computer Science, Massachusetts Institute of Technology, Cambridge, MA 02139 USA.

Color versions of one or more of the figures in this paper are available online at http://ieeexplore.ieee.org.

Digital Object Identifier 10.1109/TMTT.2017.2785842

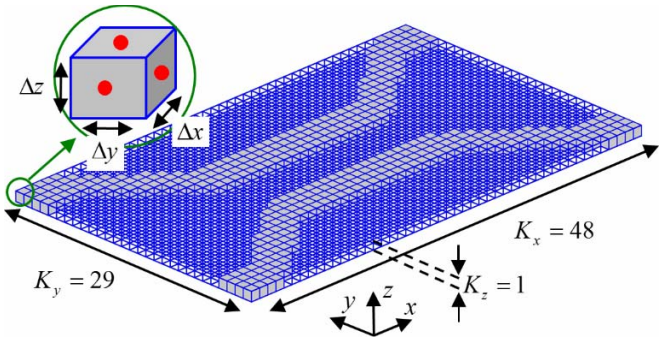

Fig. 1. Geometry description of an example voxelized geometry: gray boxes are nonempty (conductor) voxels, each of which has six nodes (indicate by red dots) on its surfaces.

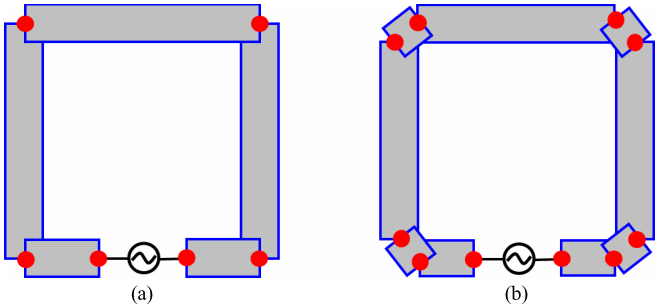

Fig. 2. Realization of a square coil in FastHenry. The conductors around corners are connected via either (a) nodes (indicated by red dots) or (b) tilted conductors.

its application to the inductance analysis of various structures including conductors with square cross section, round wires, square and circular coils, and arrays of square coils and RF inductors (situated above ground planes). It is worth mentioning that the FastHenry simulator is not suitable for inductance extraction of voxelized geometries since its basis functions are not sufficient to preserve the current continuity around the corners in voxelized settings (as explained in Section II-B). It should be noted here that the proposed VoxHenry inductance extractor is described in detailed for the first time in this paper. A presentation, which outlines the basic principles underlying the simulator, was given at an earlier symposium [10].

II. Formulation and Discretization

Let V' denote the volume of a structure comprising of conductor(s) with conductivity σ and residing in free space with permittivity ε_0 and permeability μ_0. The conductor(s) is/are excited by source(s) operated at angular frequencies $\omega_i = 2\pi f_i$, and $i = 1, \ldots, N_f$, where f_i denotes the frequency point and N_f is the number of frequency points.

In a voxelized geometry setting (Fig. 1), the volume of structure V' is enclosed by a bounding box that consists of K_t voxels; $K_t = K_x \times K_y \times K_z$, where K_x, K_y, and K_z denote the number of voxels along x-, y-, and z-directions, respectively. In Fig. 1, while some of voxels are empty, the rest of voxels are nonempty and enclosed by the conductor. Total number of nonempty voxels is represented by K. Each voxel has the size of Δx, Δy, and Δz along x-, y-, and z-directions, respectively. (Note that we assume $\Delta x = \Delta y = \Delta z$ throughout this paper.) Each nonempty voxel has nodes defined on the centers of its six surfaces. Some nodes are shared by adjacent voxels and the total number of unique nodes on the structure is M.

A. Integral Equations

The proposed VoxHenry simulator solves the mixed potential electric VIE along with the current conservation law [9], [11], which reads

$$\frac{\mathbf{J}(\mathbf{r})}{\sigma} + j\omega\mu_0 \int_{V'} G(\mathbf{r}, \mathbf{r}')\mathbf{J}(\mathbf{r}')dv' = -\nabla\Phi(\mathbf{r}) \quad (1)$$

$$\nabla \cdot \mathbf{J}(\mathbf{r}) = 0. \quad (2)$$

Here $G(\mathbf{r}, \mathbf{r}') = 1/(4\pi|\mathbf{r} - \mathbf{r}'|)$ is the free space Green's function, $\mathbf{r}$ and $\mathbf{r}'$ denote observation and source locations in V', and $\mathbf{J}(\mathbf{r})$ and $\Phi(\mathbf{r})$ represent the vector current density and the scalar potential, respectively. Equations (1) and (2) are solved simultaneously for the vector of current densities $\mathbf{J}(\mathbf{r})$, and the vector of scalar potentials $\Phi(\mathbf{r})$ in order to obtain the frequency-dependent inductance and resistance of a structure.

B. Basis Functions and Discretization

In the magneto-quasistatic case, currents within conductors are assumed to flow parallel to the conductor surfaces while no charge accumulates on the surfaces [12]. Therefore, FastHenry leverages (divergence-free) piecewise-constant basis functions to approximate the current density and assure no charge accumulation within or on the structure. However, piecewise-constant basis functions are insufficient to represent current flow around corners and additional basis functions are needed to satisfy the current conservation law. To make the current turn the corners "manually" in FastHenry, care must be taken while defining the structure. For an example scenario of a square coil, the conductors around the corners are to be connected through either nodes [Fig. 2(a)] or "tilted" conductors [Fig. 2(b)] to ensure the current continuity on the corners. Note that both these special treatments require overlap of the conductors. Nevertheless, none of these treatments are applicable to voxelized conductors as voxels cannot overlap due to their alignment on the structured 3-D grid.

To ensure the current continuity throughout the voxelized conductors in VoxHenry, the current density is approximated in terms of piecewise-constant and piecewise-linear basis functions as

$$\mathbf{J}(\mathbf{r}) \approx \sum_{k=1}^{K} I_k^x \mathbf{f}_k^x(\mathbf{r}) + I_k^y \mathbf{f}_k^y(\mathbf{r}) + I_k^z \mathbf{f}_k^z(\mathbf{r}) + I_k^{2D} \mathbf{f}_k^{2D}(\mathbf{r}) + I_k^{3D} \mathbf{f}_k^{3D}(\mathbf{r}) \quad (3)$$

where $\mathbf{f}_k^x(\mathbf{r})$, $\mathbf{f}_k^y(\mathbf{r})$, and $\mathbf{f}_k^z(\mathbf{r})$ are the piecewise-constant basis functions; $\mathbf{f}_k^{2D}(\mathbf{r})$ and $\mathbf{f}_k^{3D}(\mathbf{r})$ are the piecewise-linear basis functions. I_k^x, I_k^y, I_k^z, I_k^{2D}, and I_k^{3D} are their corresponding unknown coefficients. The basis functions are defined as

$$\mathbf{f}_k^x(\mathbf{r}) = \hat{\mathbf{x}} \quad \mathbf{f}_k^y(\mathbf{r}) = \hat{\mathbf{y}} \quad \mathbf{f}_k^z(\mathbf{r}) = \hat{\mathbf{z}} \quad (4)$$

$$\mathbf{f}_k^{2D}(\mathbf{r}) = ((x - x_k)\hat{\mathbf{x}} - (y - y_k)\hat{\mathbf{y}})/\Delta x \quad (5)$$

$$\mathbf{f}_k^{3D}(\mathbf{r}) = ((x - x_k)\hat{\mathbf{x}} + (y - y_k)\hat{\mathbf{y}} - 2(z - z_k)\hat{\mathbf{z}})/\Delta x. \quad (6)$$

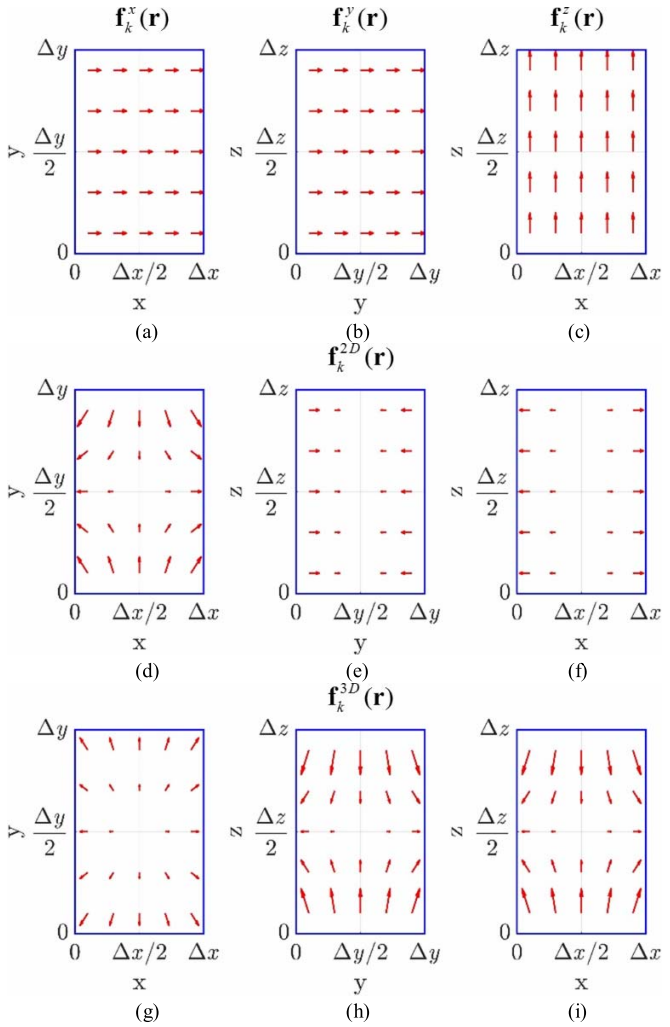

Fig. 3. Plot of piecewise-constant basis functions (a) $\mathbf{f}_k^x(\mathbf{r})$ on xy cut, (b) $\mathbf{f}_k^y(\mathbf{r})$ on yz cut, and (c) $\mathbf{f}_k^z(\mathbf{r})$ on xz cut. The plot of piecewise-linear basis function $\mathbf{f}_k^{2D}(\mathbf{r})$ on (d) xy cut, (e) yz cut, and (f) xz cut. The plot of piecewise-linear basis function $\mathbf{f}_k^{3D}(\mathbf{r})$ on (g) xy cut, (h) yz cut, and (i) xz cut.

Here (x_k, y_k, z_k) are the coordinates of the center of kth nonempty voxel. All basis functions are divergence-free and orthogonal to each other, i.e.,

$$\nabla \cdot \mathbf{f}_k^{\alpha}(\mathbf{r}) = 0 \tag{7}$$

$$\int_{V_k} \mathbf{f}_k^{\beta}(\mathbf{r}) \cdot \mathbf{f}_k^{\alpha}(\mathbf{r}) dV = 0, \quad \alpha \neq \beta \tag{8}$$

where $\alpha, \beta \in \{x, y, z, 2D, 3D\}$, V_k is the volume of kth nonempty voxel. In Fig. 3, the basis functions are plotted on cuts passing through the center of an example voxel. Clearly, the piecewise-constant basis functions, $\mathbf{f}_k^x(\mathbf{r})$, $\mathbf{f}_k^y(\mathbf{r})$, and $\mathbf{f}_k^z(\mathbf{r})$, constitute 1-D currents inside the voxel [Fig.3(a)–(c)], while the piecewise-linear basis functions, $\mathbf{f}_k^{2D}(\mathbf{r})$ and $\mathbf{f}_k^{3D}(\mathbf{r})$, support 2-D and 3-D currents inside the voxel [Fig. 3(d)–(i)], which make the current turn the corners in a voxelized setting. It is worth mentioning here that the current density in each nonempty voxel is represented by five basis functions, resulting in $N = 5K$ basis functions to represent the current density on the structure. In case, linear basis functions' set presented in [13] was used, twelve basis functions would be required to represent the current density in each voxel. Therefore, the selected basis function set appears to have minimal elements while allowing first-order approximation to the current density.

Next, substituting (3) into (1), testing the resulting equation with (4)–(6) and enforcing the continuity of the normal component of the current density across M voxel surfaces yield a linear system of equations with dimensions $(N+M)\times(N+M)$ as

$$\begin{bmatrix} \mathbf{V} \\ 0 \end{bmatrix} = \begin{bmatrix} \overline{\mathbf{Z}} & -\overline{\mathbf{A}}^T \\ \overline{\mathbf{A}} & 0 \end{bmatrix} \begin{bmatrix} \mathbf{I} \\ \mathbf{\Phi} \end{bmatrix}. \tag{9}$$

Note that 1) the continuity condition of the current density's normal component is obtained from the integral form of (2) and 2) differential form as given in (2) is satisfied everywhere (except the voxel surfaces) since all basis functions are divergence free. In (9), the unknown current coefficient vector $\mathbf{I}$ is constructed by concatenating the column vectors of unknown coefficients pertinent to each group of basis functions, i.e., $\mathbf{I} = [\mathbf{I}^x; \mathbf{I}^y; \mathbf{I}^z; \mathbf{I}^{2D}; \mathbf{I}^{3D}]$. The entries of $\mathbf{I}$ are provided in Appendix A. The discretization method used here does not require the scalar potential to be represented in terms of basis functions. The scalar potential is sampled at the center of every voxel surface, where it is assumed constant. These constants are represented by Φ_m, $m = 1, \ldots, M$, the entries of unknown potential coefficient vector $\mathbf{\Phi}$. The entries of excitation vector $\mathbf{V}$ are obtained using the procedure explained in Section II-C. In (9), $\overline{\mathbf{Z}}$ is the method of moments (MoM) matrix and can be written explicitly as

$$\overline{\mathbf{Z}} = \begin{bmatrix} \overline{\mathbf{Z}}^{x,x} & 0 & 0 & \overline{\mathbf{Z}}^{x,2D} & \overline{\mathbf{Z}}^{x,3D} \\ 0 & \overline{\mathbf{Z}}^{y,y} & 0 & \overline{\mathbf{Z}}^{y,2D} & \overline{\mathbf{Z}}^{y,3D} \\ 0 & 0 & \overline{\mathbf{Z}}^{z,z} & 0 & \overline{\mathbf{Z}}^{z,3D} \\ \overline{\mathbf{Z}}^{2D,x} & \overline{\mathbf{Z}}^{2D,y} & 0 & \overline{\mathbf{Z}}^{2D,2D} & \overline{\mathbf{Z}}^{2D,3D} \\ \overline{\mathbf{Z}}^{3D,x} & \overline{\mathbf{Z}}^{3D,y} & \overline{\mathbf{Z}}^{3D,z} & \overline{\mathbf{Z}}^{3D,2D} & \overline{\mathbf{Z}}^{3D,3D} \end{bmatrix} \tag{10}$$

where $\overline{\mathbf{Z}}$ is a complex symmetric matrix which can be expressed as $\overline{\mathbf{Z}} = \overline{\mathbf{R}} + j\omega\overline{\mathbf{L}}$, $\overline{\mathbf{R}}$ is a diagonal matrix of dc resistances, and $\overline{\mathbf{L}}$ is a symmetric matrix of partial inductances [9], [14], [15]. The entries of the blocks in $\overline{\mathbf{Z}}$, which are represented as $\overline{\mathbf{Z}}^{\beta,\alpha}$, $\beta, \alpha \in \{x, y, z, 2D, 3D\}$, are obtained by testing the left-hand side of (1) with $\mathbf{f}^{\beta}(\mathbf{r})$ after $\mathbf{J}(\mathbf{r})$ is expanded in terms of $\mathbf{f}^{\alpha}(\mathbf{r})$ on all nonempty voxels, as explained in Appendix A.

The matrix $\overline{\mathbf{A}}$ is the incidence matrix with dimensions $M \times N$ and enforces the continuity of the current density's normal component across voxel surfaces [9], [11]. Each row of $\overline{\mathbf{A}}$ corresponds to one node while each column of $\overline{\mathbf{A}}$ corresponds to one basis function. The entry in mth row and nth column of $\overline{\mathbf{A}}$ is the contribution of the current modeled by the nth basis function to the mth node. If no link exists between them, it is zero. Otherwise the value of the $\overline{\mathbf{A}}$ matrix entry is determined due to the value of basis function at mth node and entrance/exit status of the current associated with nth basis function. The value of the entry is multiplied by -1, if the current exiting from the node or $+1$ if the current is entering to the node. (Note that the entries of $\overline{\mathbf{A}}^T$, transpose of $\overline{\mathbf{A}}$, are also provided in Appendix A.)

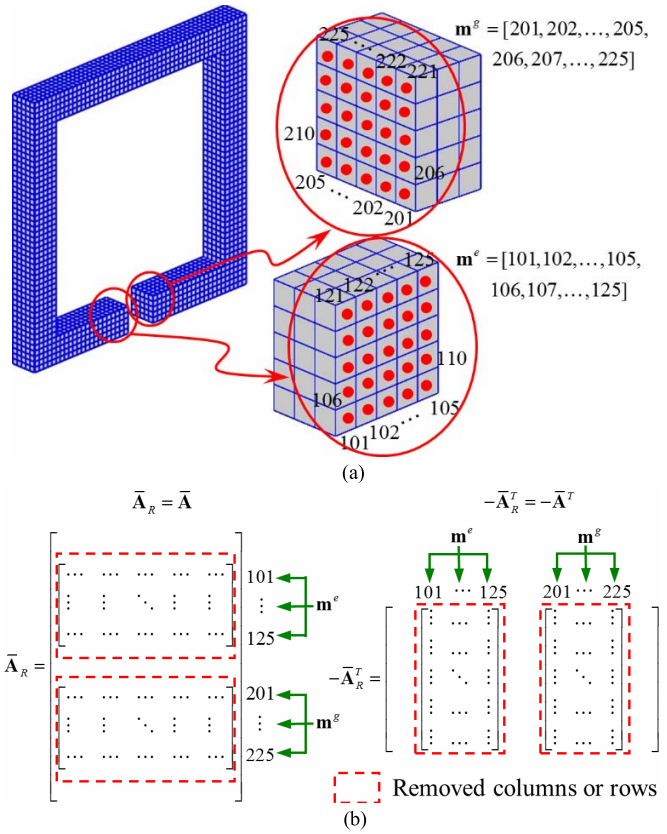

Fig. 4. For an example scenario of a square coil, (a) port nodes that consist of excitation nodes $\mathbf{m}^e$ and ground nodes $\mathbf{m}^g$ and their ids and (b) modifications in $\overline{\mathbf{A}}_R$ and $-\overline{\mathbf{A}}_R^T$ matrices for defining the boundary conditions.

To obtain inductance and resistance of the structure, the linear system of equations in (9) is solved iteratively for $\mathbf{I}$ and $\mathbf{\Phi}$. During the iterative solution, the MVMs involving $\overline{\mathbf{A}}$ is computationally cheap as $\overline{\mathbf{A}}$ is a sparse matrix with only a couple of nonzero entries in each column. The computational complexity of multiplications with $\overline{\mathbf{A}}$ scales with $O(N)$. On the other hand, the MVMs involving $\overline{\mathbf{Z}}$ is computationally expensive as the blocks in $\overline{\mathbf{Z}}$, $\overline{\mathbf{Z}}^{\beta,\alpha}$, are full matrices with dimensions $K \times K$. The multiplication with each block $\overline{\mathbf{Z}}^{\beta,\alpha}$ requires $O(K^2)$ operations, which is reduced to $O(K_t \log K_t)$ via the FFT acceleration technique explained in Section III-B.

C. Boundary Conditions and Excitation

In VoxHenry, excitations are defined by properly setting the boundary conditions on the nodes. In general, either current sources or voltage sources can be defined and connected to the nodes in a port. Here, we focus on the implementation of a voltage source as its implementation yields a symmetric linear system of equations.

To define a voltage source in a port, port nodes and their ids are identified first. For an example scenario of a square coil, the port nodes and their ids are shown in Fig. 4(a). These port nodes consist of excitation nodes and ground nodes; their ids are stored in vectors $\mathbf{m}^e$ and $\mathbf{m}^g$, respectively [Fig. 4(a)]. Next, the matrices $\overline{\mathbf{A}}$ and $-\overline{\mathbf{A}}^T$ are duplicated as $\overline{\mathbf{A}}_R$ and $-\overline{\mathbf{A}}_R^T$, respectively. For ground nodes, all rows in $\overline{\mathbf{A}}_R$ and all columns in $-\overline{\mathbf{A}}_R^T$ which correspond to ids in $\mathbf{m}^g$ are removed from $\overline{\mathbf{A}}_R$ and $-\overline{\mathbf{A}}_R^T$ matrices. The same operation is applied for the excitation nodes using $\mathbf{m}^e$ after adding all columns in $-\overline{\mathbf{A}}_R^T$ corresponding to ids in $\mathbf{m}^e$ to each other and assigning the resulting column vector to $\mathbf{V}$. (Note that the procedure to obtain $-\overline{\mathbf{A}}_R^T$ as well as $\mathbf{V}$ from the columns of $-\overline{\mathbf{A}}^T$ is detailed in Algorithm I.) The modifications in $\overline{\mathbf{A}}_R$ and $-\overline{\mathbf{A}}_R^T$ matrices for defining boundary conditions in the example scenario of a square coil are demonstrated in Fig. 4(b). It should be noted that the modifications in $\overline{\mathbf{A}}_R$ and $-\overline{\mathbf{A}}_R^T$ matrices allow preserving the symmetry in system matrix, and hence enable to use a memory efficient preconditioner explained in Section III-A. (Note that although the numbers of rows and columns in $\overline{\mathbf{A}}_R$ and $-\overline{\mathbf{A}}_R^T$, respectively, are smaller than M, we assume them as M in the rest of this paper for the sake of simplicity since the number of port nodes is often very small compared to the total number of unique nodes.)

Algorithm 1 Pseudocode for Generating $-\overline{\mathbf{A}}_R^T$ and $\mathbf{V}$ from $-\overline{\mathbf{A}}^T$

```
V = zeros(N + M, 1)
for k = 1 : length(m^e)
    V(1 : N, 1) = V(1 : N, 1) − Ā^T(:, m^e(k))
end for
−Ā_R^T(:, :) = −Ā^T(:, :)
−Ā_R^T(:, [m^e(:) m^g(:)]) = [ ]
return V and −Ā_R^T
```

In VoxHenry, the $L \times L$ magneto-quasistatic port admittance matrix, $\overline{\mathbf{Y}}_P$, for an L port structure is computed one column at a time for a given frequency. For the structures with single port ($L = 1$), the self-resistance and self-inductance of the structure are obtained by exciting the port by a voltage source and computing the currents on the port. The admittance (and hence impedance) of the structure is computed by multiplying the column vector of the solution, $[\mathbf{I}; \mathbf{\Phi}]$, with row vector $\mathbf{V}^T$. For the structures with L ports ($L > 1$), the impedance matrix, $\overline{\mathbf{Z}}_P$, ($\overline{\mathbf{Z}}_P = \overline{\mathbf{Y}}_P^{-1}$) tabulating the self- and mutual resistances and inductances of all ports is obtained by L number of simulations. In each simulation, the voltage source is connected to one port while the nodes in the remaining ports are connected to the ground. Then, the currents on all ports are computed and one column of the admittance matrix $\overline{\mathbf{Y}}_P$ for the structure is obtained by multiplying the column vector of the solution $[\mathbf{I}; \mathbf{\Phi}]$ with the row vector $\mathbf{V}^T$ pertinent to the considered port at each simulation. In a succinct way, this operation can be expressed as

$$\overline{\mathbf{Y}}_P = \begin{bmatrix} \cdots & \mathbf{V}_l^T & \cdots \end{bmatrix} \begin{bmatrix} \overline{\mathbf{Z}} & -\overline{\mathbf{A}}_R^T \\ \overline{\mathbf{A}}_R & 0 \end{bmatrix}^{-1} \begin{bmatrix} \vdots \\ \mathbf{V}_l \\ \vdots \end{bmatrix} \quad (11)$$

where $l = 1, \ldots, L$, $\overline{\mathbf{Y}}_P$ is complex symmetric since $\overline{\mathbf{A}}_R$ and $\mathbf{V}$ are real and $\overline{\mathbf{Z}}$ is complex symmetric. For the structures with single conductor, defining a port and connecting at least one node in the port to the ground eliminates the static null space of dimension one, which gives

rise to slow convergence of the iterative solution of the linear system of equations in (9). For the structures comprising of several separate conductors, the potential of one node on each conductor has to be set to zero to eliminate the nullspaces associated with each conductor.

III. Numerical Solution

A. Sparse Preconditioner

To ensure the rapid convergence of iterative solution of (9), FastHenry utilizes a mesh-based approach in conjunction with a local-inversion preconditioner [9] along with other positive definite extensions. That said, implementation of mesh-based approach for the VoxHenry appears to be nontrivial due to the existence of the piecewise-linear basis functions in the basis function set. Therefore, we here propose a sparse preconditioner to accelerate the iterative convergence of VoxHenry, which reads

$$\overline{\mathbf{P}} = \overline{\mathbf{O}}^{-1} = \begin{bmatrix} \overline{\mathbf{Y}} & -\overline{\mathbf{A}}_R^T \\ \overline{\mathbf{A}}_R & 0 \end{bmatrix}^{-1} \tag{12}$$

where $\overline{\mathbf{Y}}$ is a diagonal matrix with entries corresponding to magnitudes of diagonal entries of $\overline{\mathbf{Z}}$. During the iterative solution of (9), the sparse preconditioner $\overline{\mathbf{P}}$ is applied to both sides of (9) as

$$\begin{bmatrix} \overline{\mathbf{Y}} & -\overline{\mathbf{A}}_R^T \\ \overline{\mathbf{A}}_R & 0 \end{bmatrix}^{-1} \begin{bmatrix} \mathbf{V} \\ 0 \end{bmatrix} = \begin{bmatrix} \overline{\mathbf{Y}} & -\overline{\mathbf{A}}_R^T \\ \overline{\mathbf{A}}_R & 0 \end{bmatrix}^{-1} \begin{bmatrix} \overline{\mathbf{Z}} & -\overline{\mathbf{A}}_R^T \\ \overline{\mathbf{A}}_R & 0 \end{bmatrix} \begin{bmatrix} \mathbf{I} \\ \mathbf{\Phi} \end{bmatrix}. \tag{13}$$

To perform the multiplications with sparse preconditioner, the standard application of Schur complement [16] to the solution of linear systems of equations can be leveraged. To do that, let the column vector [**a**; **b**] represents the result of MVM at the right-hand side of (9) at each iteration. The multiplication of the column vector with the sparse preconditioner results in a column vector [**c**; **d**], i.e.,

$$\begin{bmatrix} \mathbf{c} \\ \mathbf{d} \end{bmatrix} = \begin{bmatrix} \overline{\mathbf{Y}} & -\overline{\mathbf{A}}_R^T \\ \overline{\mathbf{A}}_R & 0 \end{bmatrix}^{-1} \begin{bmatrix} \mathbf{a} \\ \mathbf{b} \end{bmatrix}. \tag{14}$$

The resulting column vector [**c**; **d**] is obtained in two steps: in the first step, **d** is obtained as

$$\mathbf{d} = \overline{\mathbf{S}}^{-1}(\mathbf{b} - \overline{\mathbf{A}}_R \overline{\mathbf{Y}}^{-1}\mathbf{a}) \tag{15}$$

where $\overline{\mathbf{S}}$ is the Schur complement of the block $\overline{\mathbf{Y}}$ of the matrix $\overline{\mathbf{O}}$, i.e., $\overline{\mathbf{S}} = \overline{\mathbf{A}}_R \overline{\mathbf{Y}}^{-1} \overline{\mathbf{A}}_R^T$. In the second step, **c** is obtained using **d** as

$$\mathbf{c} = \overline{\mathbf{Y}}^{-1}(\mathbf{a} + \overline{\mathbf{A}}_R^T \mathbf{d}). \tag{16}$$

In (15) and (16), computing the inverse of $\overline{\mathbf{Y}}$ is trivial as $\overline{\mathbf{Y}}$ is a diagonal matrix. In addition, inversion of Schur complement $\overline{\mathbf{S}}$ requires minimal computational resources when performed with LDLT decomposition in Suitesparse package [17] since $\overline{\mathbf{S}}$ is a sparse, positive definite, and symmetric real matrix. The effectiveness of the proposed sparse preconditioner is demonstrated in the numerical example in Section IV-A4, in which the number of iterations is a few at low frequencies while that is around twenty at the maximum frequency.

B. FFT Acceleration

As discussed in Section II-B, the computational cost of MVMs involving the blocks in $\overline{\mathbf{Z}}$, $\overline{\mathbf{Z}}^{\beta,\alpha}$, can be reduced from $O(K^2)$ to $O(K_t \log K_t)$ by using FFTs. To do that, the block Toeplitz tensors $\mathcal{G}^{\beta,\alpha}$, $\beta, \alpha = \{x, y, z, 2D, 3D\}$, corresponding to the blocks of MoM matrix in (10), $\overline{\mathbf{Z}}^{\beta,\alpha}$, $\beta, \alpha \in \{x, y, z, 2D, 3D\}$ are obtained. Next, each block Toeplitz tensor $\mathcal{G}^{\beta,\alpha}$ with dimensions $K_x \times K_y \times K_z$ is embedded in a block circulant tensor $\mathcal{C}^{\beta,\alpha}$ with dimensions $2K_x \times 2K_y \times 2K_z$; the procedure to obtain each block Toeplitz and circulant tensor is expounded in Appendix B. Once the FFTs of all circulant tensors $\mathcal{C}^{\beta,\alpha}$ corresponding to $\overline{\mathbf{Z}}^{\beta,\alpha}$ are computed and stored in $\tilde{\mathcal{C}}^{\beta,\alpha}$, those are used to compute MVM involving $\overline{\mathbf{Z}}^{\beta,\alpha}$, which is $\mathbf{CC}^\beta = \overline{\mathbf{Z}}^{\beta,\alpha}\mathbf{I}^\alpha$, as

$$\mathcal{CC}^\beta = c^\beta \mathcal{I}^\beta + \text{IFFT}\left\{ \sum_\alpha \tilde{\mathcal{C}}^{\beta,\alpha} * \tilde{\mathcal{I}}^\alpha \right\}. \tag{17}$$

Here $*$ and IFFT stand for tensor–tensor multiplication and inverse FFT operator, $\mathcal{I}^\alpha$ is the tensor with dimensions $2K_x \times 2K_y \times 2K_z$ that contains the unknown current coefficients corresponding the basis function $\mathbf{f}^\alpha(\mathbf{r})$, and $\tilde{\mathcal{I}}^\alpha = \text{FFT}\{\mathcal{I}^\alpha\}$. c^β is a constant which equals to $1/(\sigma \Delta x)$ for $\beta = \{x, y, z\}$, $1/(\sigma 6 \Delta x)$ for $\beta = 2D$, and $1/(\sigma 2 \Delta x)$ for $\beta = 3D$. Before tensor–tensor multiplication, $\mathcal{I}^\alpha$ should be properly filled via $\mathbf{I}^\alpha$ and zeros. After the multiplication, the result $\mathbf{CC}^\beta$ should be selected from the entries of $\mathcal{CC}^\beta$. It is worth noting that the memory required to store all $\tilde{\mathcal{C}}^{\beta,\alpha}$ scales as $O(K_t)$. On the other hand, if the conventional MoM scheme was used, the memory for storing all $\overline{\mathbf{Z}}^{\beta,\alpha}$ would scale as $O(K^2)$, which is prohibitive for large-scale problems. To validate the computational complexity and memory scaling of the FFT accelerated simulator, the computational time required for the MVMs involving $\overline{\mathbf{Z}}$ and the memory requirement for storing all circulant tensors in each numerical example of Section IV are shown in Fig. 5(a) and (b). Needless to say, wall time for the MVMs for all numerical examples scales with $O(K_t \log K_t)$ [Fig. 5(a)], while the memory required to store all $\tilde{\mathcal{C}}^{\beta,\alpha}$ for all numerical examples scales with $O(K_t)$ [Fig. 5(b)].

IV. Numerical Results

This section presents several numerical results that demonstrate the accuracy, efficiency, and applicability of the VoxHenry simulator. In all examples below, the conductivity of the conductors is set to 5.8×10^7 S/m and the structures are excited by voltage sources. When applicable, the results obtained by VoxHenry are compared with those obtained by FastHenry or analytical expressions. The discrepancy between results are quantified through L^2 norm error, which is defined as

$$\text{err} = \sqrt{\sum_{i=1}^{N_f} |F(f_i) - \tilde{F}(f_i)|^2 \Big/ \sum_{i=1}^{N_f} |\tilde{F}(f_i)|^2} \tag{18}$$

where F denotes the quantity of interest (e.g., inductance and resistance) computed by VoxHenry while $\tilde{F}$ represents the quantity of interest computed either by FastHenry or analytical expression, unless stated otherwise. All simulations are performed on an Intel Xeon CPU E5-2680 v4 processor.

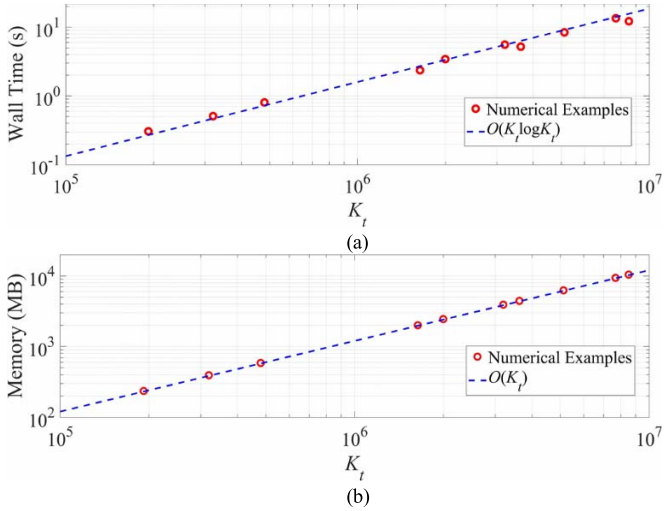

Fig. 5. (a) Computational time for MVM involving $\overline{\mathbf{Z}}$ and (b) memory requirement for storing all circulant tensors in numerical examples in Section IV.

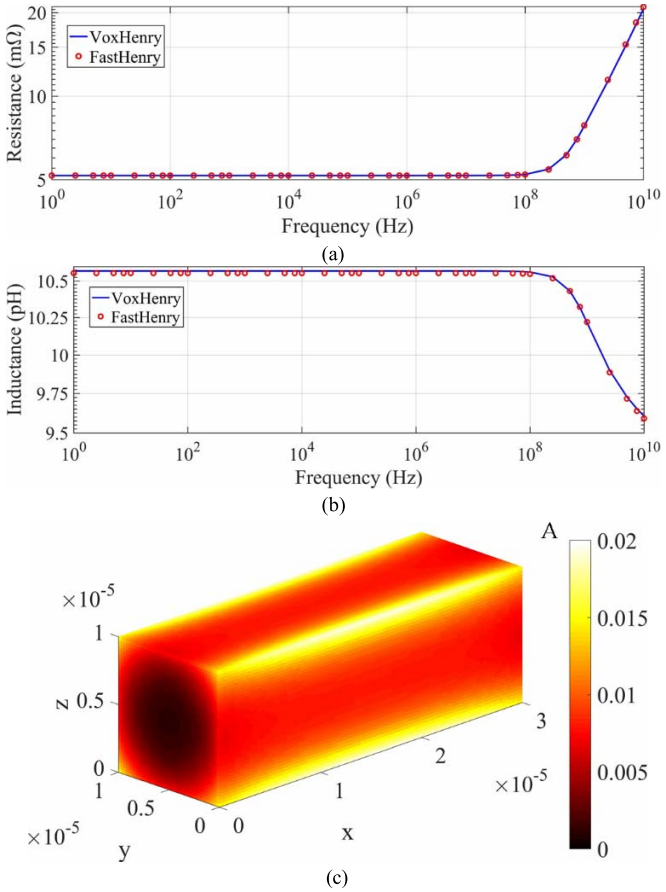

Fig. 6. Frequency-dependent (a) resistance and (b) inductance of a straight conductor with square cross section computed via VoxHenry and FastHenry. (c) Current distribution on the structure at 2.5 GHz.

A. Validation Examples

1) Straight Conductor With Square Cross Section: VoxHenry and FastHenry are used to obtain frequency-dependent resistance and inductance of a straight conductor with dimensions $10 \times 10 \times 30$ μm (width $\times$ height $\times$ length). The structure is connected to a port from both ends and excited at frequencies ranging from 1 Hz to 10 GHz (four equally spaced frequency points at each decade). The structure is discretized by voxels of size 0.25 μm, which gives rise to $N = 960\,000$ and $M = 587\,200$. In Fig. 6(a) and (b), the frequency-dependent resistance and inductance obtained by VoxHenry are compared with those obtained by FastHenry. Perfect agreement between results is observed; the L^2 norm error between the results is computed as 0.010 and 0.0013 for the resistance and inductance, respectively. Furthermore, the current distribution on the structure at 2.5 GHz is shown in Fig. 6(c) and the skin effect is clearly observed. It should be noted that the VoxHenry computes the frequency-dependent inductance and resistance at 41 frequency points in 20.5 min, which shows the efficiency of VoxHenry for a structure discretized with 192 000 voxels.

2) Wire: Next, the frequency-dependent resistance and inductance of a wire with length 50 μm and radius 5 μm are computed using VoxHenry and FastHenry. The structure is connected to a port from both ends and excited at frequencies ranging from 1 Hz to 10 GHz (four equally spaced frequency points at each decade). The structure is discretized by voxels of size 0.2 μm ($N = 2\,470\,000$ and $M = 1\,508\,976$), 0.25 μm ($N = 1\,264\,000$ and $M = 775\,664$), 0.5 μm ($N = 158\,000$ and $M = 99\,116$), and 1.0 μm ($N = 20\,000$ and $M = 13\,080$). The frequency-dependent resistance and inductance of the wire discretized with voxels of size 0.25 μm are computed by the VoxHenry, FastHenry, and analytical expressions [18] [Fig. 7(a) and (b)]. The L^2 norm error (with respect to the analytical solution) in resistance and inductance computed by the VoxHenry is 0.063 and 0.0062, and in those computed by the FastHenry is 0.062 and 0.006, respectively. It should be noted here that for both simulators, L^2 norm error, which is computed with respect to analytical solution, does not decrease when the voxel size is reduced to 0.2 μm. This can be explained by the fact that the accuracy of the analytical expressions is limited due to the approximations used during their derivation. To this end, resistance and inductance values obtained by the VoxHenry and FastHenry for the wire discretized with voxels of size 0.2 μm are used as the reference solutions [$\tilde{F}$ in (18)] to compute L^2 norm errors. For the wire discretized with voxels of size $\{1.0, 0.5, 0.25\}$ μm, L^2 norm errors in resistance and inductance are found to be $\{3.02, 0.13, 0.11\} \times 10^{-2}$ and $\{4.18, 0.36, 0.04\} \times 10^{-3}$ for the VoxHenry and $\{3.18, 1.33, 0.11\} \times 10^{-2}$ and $\{4.74, 2.64, 0.06\} \times 10^{-3}$ for the FastHenry. The accuracy of the solutions obtained by both of the simulators exhibit a similar convergence rate. Simulation times required by the VoxHenry and FastHenry to compute the resistance and inductance at 41 frequency points are $\{0.20, 2.26, 33.12, 112.21\}$ and $\{0.18, 3.43, 64.63, 202.45\}$ min, respectively. Furthermore, the memory requirements of the VoxHenry and FastHenry are $\{0.03, 0.45, 11.12, 30.65\}$ and $\{0.06, 0.56, 5.45, 11.97\}$ GB, respectively. It should be noted here that the two simulators have implementation differences. While the VoxHenry executes a multithreaded MATLAB code, the FastHenry is built on a serial C code. It should also be noted that the FastHenry is not applicable to all voxelized structures (such as the one in Section IV-A6)

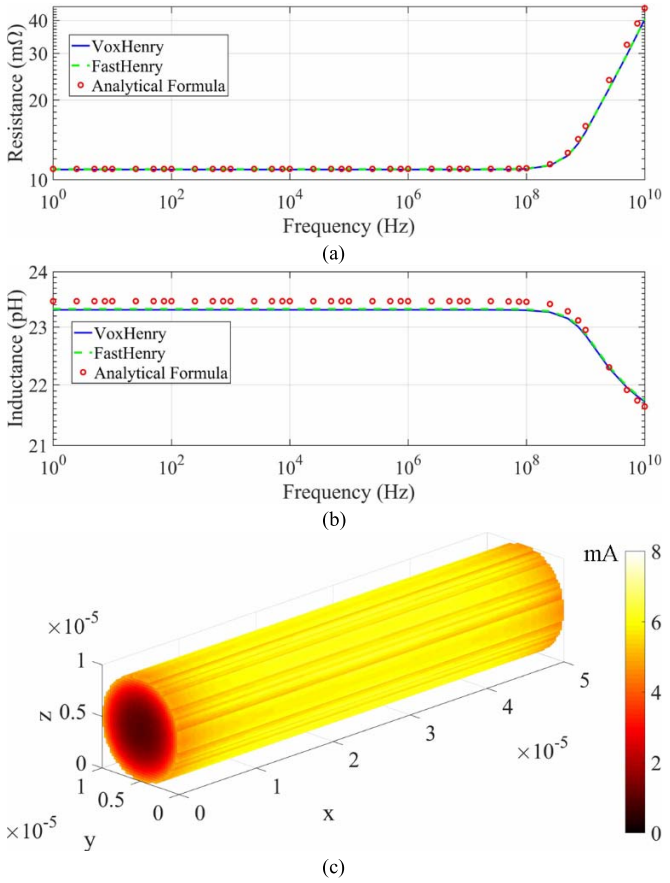

Fig. 7. Frequency-dependent (a) resistance and (b) inductance of a wire computed via VoxHenry, FastHenry, and analytical formula. (c) Current distribution on the wire at 2.5 GHz.

since it cannot assign nodes on all faces of the voxels and model the rotating currents on voxels due to corner issue explained in Section II-B. Finally, Fig. 7(c) shows the current distribution computed by the VoxHenry inside the wire discretized with voxels of size 0.25 μm. Fig. 7(c) clearly shows the skin depth phenomenon.

3) Parallel Straight Conductors: Two parallel conductors with dimensions $10 \times 5 \times 30$ μm (width $\times$ height $\times$ length) positioned 10 μm apart from each other (edge-to-edge) are considered. The conductors lie parallel to the xy plane and are connected to the ports from their ends. The structure is excited at frequencies ranging from 1 Hz to 10 GHz (four equally spaced frequency points at each decade) and discretized by voxels of size 0.25 μm ($N = 1\,600\,000$ and $M = 985\,600$). In Fig. 8(a)–(d), the frequency-dependent self-resistance, mutual resistance [19], self-inductance, and mutual inductance of a conductor obtained by VoxHenry and FastHenry are compared. Apparently, an excellent match between the results is obtained; L^2 norm error between the results is computed as 0.01, 0.008, 0.001, and 0.0009 for the self-resistance, mutual resistance, self-inductance, and mutual inductance, respectively. In Fig. 8(e), the current distribution on the structure at 2.5 GHz is plotted when it is excited from one port; the skin and proximity effects [20] on the conductors are clearly observed. Note that the VoxHenry completes the simulation at 41 frequency points in 45.75 min.

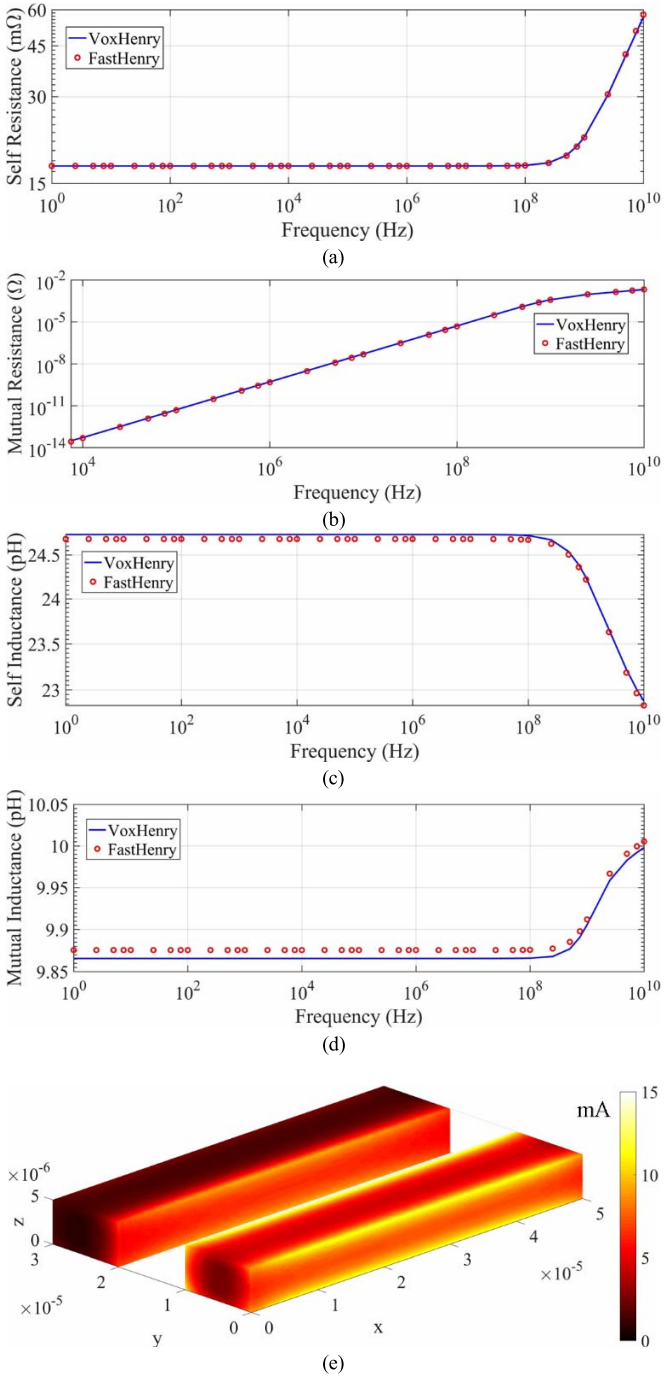

Fig. 8. In a two parallel conductor structure, the frequency-dependent (a) self-resistance, (b) mutual resistance, (c) self-inductance, and (d) mutual inductance of a conductor computed via VoxHenry and FastHenry. (Note that the frequencies below 10 kHz are not considered while plotting mutual resistance as the mutual resistance at these frequencies is less than the machine precision.) (e) Current distribution on both conductors at 2.5 GHz.

4) Square Coil: A square coil with length 100 μm, which is formed by conductors with square cross section 5×5 μm, is considered. The square coil lies on the xz plane and its lower arm is formed by two conductors with length 49 μm. The structure is connected to a port defined in the spacing between the conductors in the lower arm. The structure is excited at frequencies ranging from 1 Hz to 10 GHz (four equally spaced frequency points at each decade) and discretized by voxels of size 0.25 μm ($N = 3\,024\,000$ and $M = 1\,875\,280$).

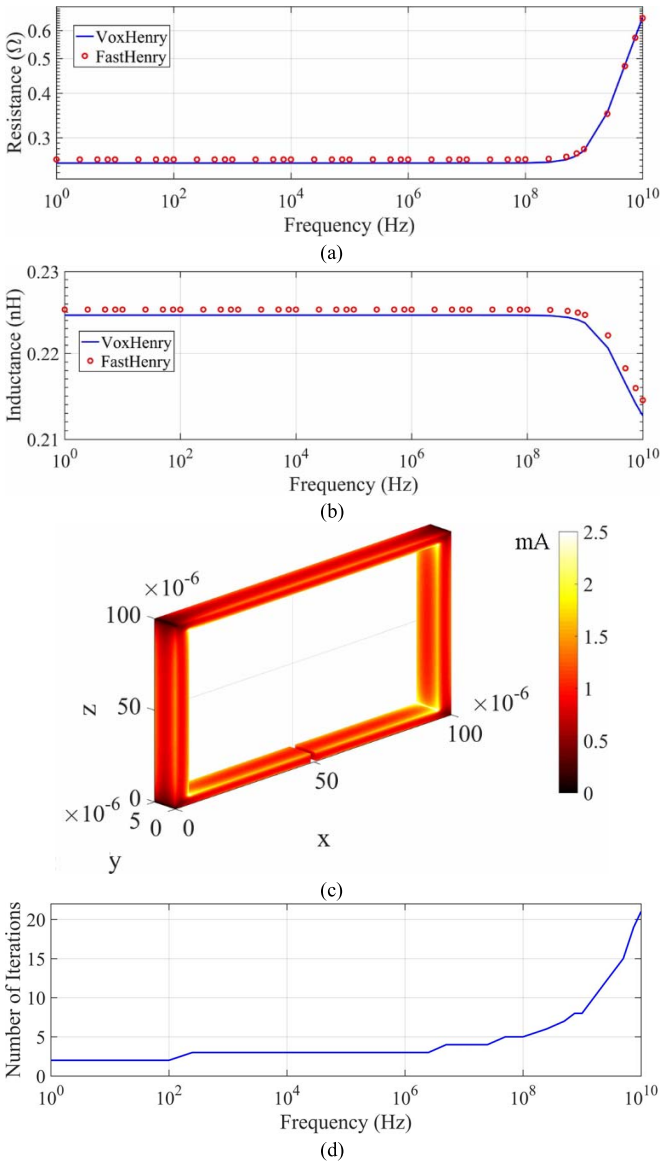

Fig. 9. Frequency-dependent (a) resistance and (b) inductance of a square coil computed via VoxHenry and FastHenry. (c) Current distribution on the square coil at 2.5 GHz. (d) Frequency versus number of iterations required to reach to relative residual error 10^{-8} during iterative solution of linear system of equations (with $N = 3\,024\,000$ and $M = 1\,875\,280$).

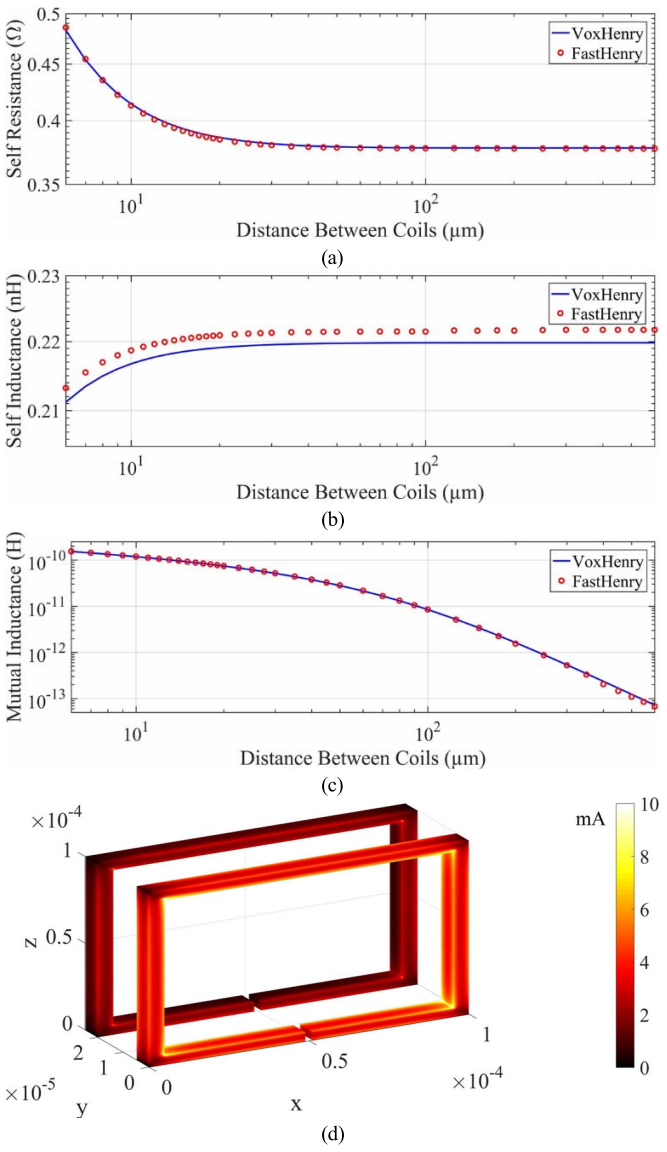

Fig. 10. Frequency-dependent (a) self-resistance, (b) self-inductance, and (c) mutual inductance of a square coil computed via VoxHenry and FastHenry. (d) Current distribution on both square coils at 3 GHz.

In Fig. 9(a) and (b), the frequency-dependent resistance and inductance of the square coil obtained by VoxHenry and FastHenry are compared. Clearly, a very good match between the results is observed; L^2 norm error between the results is computed as 0.019 and 0.0038 for the resistance and inductance, respectively. In Fig. 9(c), the current distribution on the structure at 2.5 GHz clearly shows the skin and proximity effects on the conductors. VoxHenry obtains the resistance and inductance at 41 frequency points in 47 min. For each frequency point, the number of iterations required to reach to relative residual error of 10^{-8} during the iterative solution of (9) is given in Fig. 9(d). Apparently, a couple of iterations are needed at lower frequencies while 22 iterations are need to obtain accurate solution at the highest frequency. The fast convergence of the iterative solution shows the effectiveness of the sparse preconditioner.

5) Two Parallel Square Coils: Two square coils with the specifications given in the previous numerical example are positioned parallel to each other and the spacing between them (center-to-center) is varied from 6 μm to 600 μm. Both coils are connected to ports defined in the spacing between the conductors in their lower arms and excited at 3 GHz. The structure is discretized by voxels of size 0.5 μm ($N = 756\,000$ and $M = 484\,040$). The frequency-dependent self-resistance, self-inductance, and mutual inductance of one square coil obtained by VoxHenry and FastHenry are shown in Fig. 10(a)–(c). An excellent match between results is observed; L^2 norm error between the results is calculated as 0.0029, 0.0084, and 0.0058 for the self-resistance, self-inductance, and mutual inductance, respectively. Furthermore, the current distribution on the structure is plotted when the distance between coils is 20 μm [Fig. 10(d)]. For this configuration, VoxHenry obtains the current distribution, resistance, and inductances in 4.85 min.

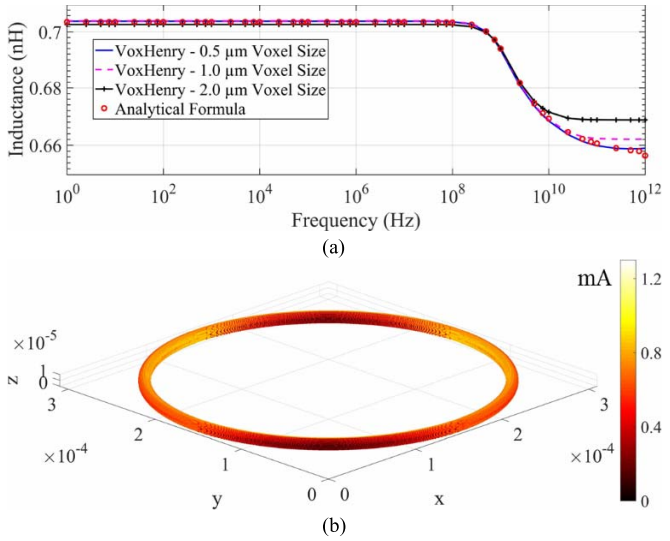

Fig. 11. (a) Frequency-dependent self-inductance of a circular coil computed via VoxHenry with different voxel sizes and analytical formula. (b) Current distribution on circular coil at 3 GHz.

6) Circular Coil: In the final validation example, a circular coil with loop radius 150 μm and tube radius 5 μm is considered. The coil is connected to a port defined in a spacing formed between $x = 155.0$ μm and $x = 155.0 + a$ μm in the lower part of the coil, where a is the voxel size, and excited at frequencies ranging from 1 Hz to 1 THz (four equally spaced frequency points at each decade). The structure is discretized by the voxels of size 0.5 μm ($N = 2\,969\,300$ and $M = 1\,867\,528$), 1 μm ($N = 373\,400$ and $M = 245\,488$), and 2 μm ($N = 47\,695$ and $M = 33\,988$). The frequency-dependent inductance of circular coil obtained by VoxHenry with different voxel sizes and analytical formula [18] are compared in Fig. 11(a). Perfect agreement between the VoxHenry and analytical results is observed for the voxel size of 0.5 μm. L^2 norm error between the analytical result and VoxHenry result for the voxel size of 0.5 μm, 1 μm, and 2 μm is obtained as 8.09×10^{-4}, 1.9×10^{-3}, and 5.4×10^{-3}, respectively. Furthermore, the current distribution on the coil obtained by VoxHenry for voxel size of 0.5 μm is shown in Fig. 11(b). It is worth mentioning that VoxHenry computes the inductance on 49 frequency points in 144, 13.5, and 2.7 min and requires 25.5, 2.64, and 0.3-GB memory for the voxel size of 0.5 μm, 1 μm, and 2 μm, respectively.

B. Large-Scale Examples

1) Square Coil Array: A 3-by-3 array of square coils with center-to-center spacing 30 μm is considered [Fig. 12(a)]. Each square coil with length 20 μm is formed by conductors with square cross section 4×4 μm and lies on the xy plane; its lower arm parallel to x-axis is formed by two conductors with length 9 μm and a port is defined in the spacing between these conductors for each coil. The coils are excited (one at a time) at frequencies ranging from 1 Hz to 10 GHz (four equally spaced frequency points at each decade). Two different scenarios are considered. In the first scenario, the coils are discretized by voxels of size 0.25 μm ($N = 2\,856\,960$ and $M = 1\,787\,904$). In the second scenario, the coils are situated over a square ground plane with dimensions $100 \times 100 \times 2$ μm (width $\times$ length $\times$ height) and whole structure is discretized by voxels of size 0.25 μm ($N = 9\,256\,960$ and $M = 5\,794\,304$); the spacing between coils and ground plane is 2 μm.

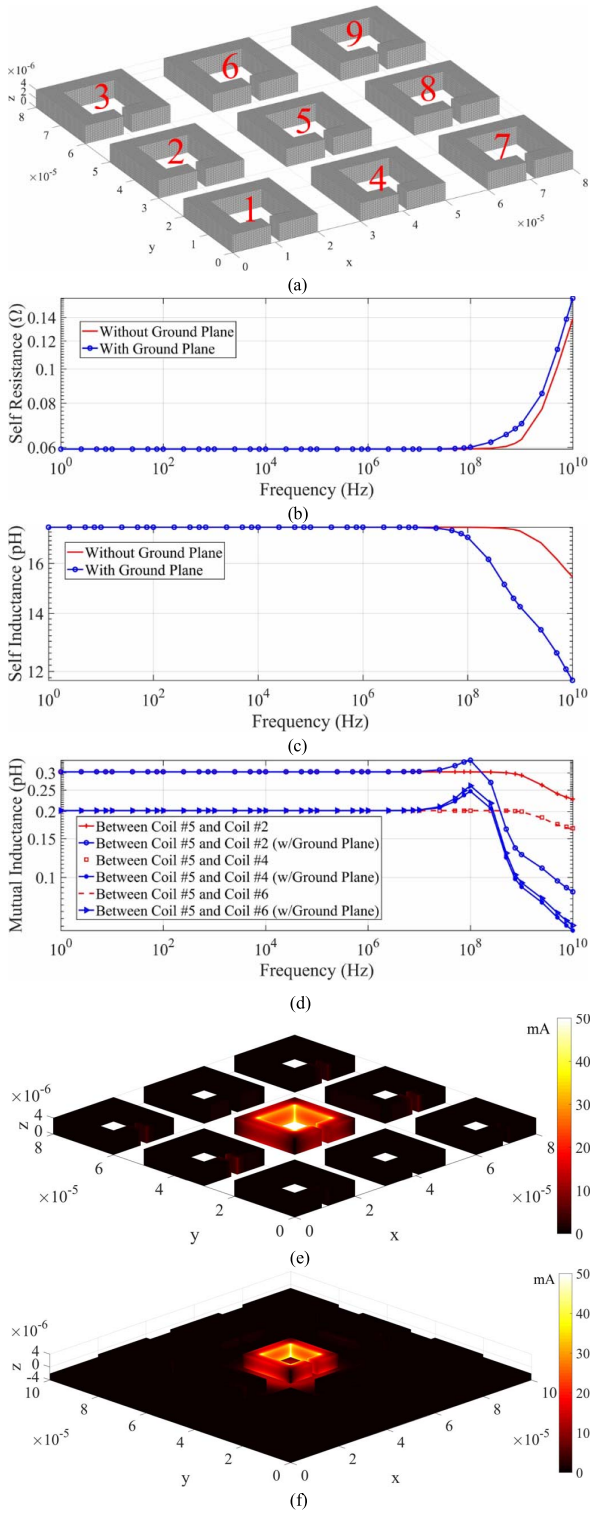

Fig. 12. (a) Geometry of square coil array. The frequency-dependent (b) self-resistance and (c) self-inductance of the fifth coil when the ground plane does not exist and exists. (d) Frequency-dependent mutual inductances of fifth coil with the second, fourth, and sixth coils when the ground plane does not exist and exists. The current distribution on the structure excited from the fifth port at 2.5 GHz when the ground plane (e) does not exist and (f) exists.

The frequency-dependent self-resistance and self-inductance of the fifth coil [i.e., the coil in the middle of array

TABLE I

DETAILED BREAKDOWN OF THE MEMORY USAGE AND WALL TIME FOR THE SQUARE COIL ARRAY EXAMPLE. UNITS FOR MEMORY AND WALL TIME ARE GB AND S.

	Square Coil Array	Square Coil Array with Ground Plane
N	2,856,960	9,256,960
M	1,787,904	5,794,304
K_t	1,638,400	5,120,000
Memory for $\overline{\mathbf{A}}_R$	0.161	0.522
Memory for $\mathcal{C}^{\beta,\alpha}$	2	6.25
Memory for LDLT decomposition of $\overline{\mathbf{S}}$	4.527	25.432
Number of iterations for solution of port #5 (tolerance=1e-8)	18	33
Time for filling out matrices & tensors	179.57	326.85
Time for iterative solution for all 9 ports	925.06	7727.26
Time for LDLT decomposition of $\overline{\mathbf{S}}$	11.27	71.55
Time for one MVM involving $\overline{\mathbf{Z}}$	2.35	8.37
Time for one MVM involving $\overline{\mathbf{P}}$	1.94	9.57
Time for one MVM involving $\overline{\mathbf{A}}_R$ and $\overline{\mathbf{A}}_R^T$	0.16	0.74

in Fig. 12(a)] obtained in both scenarios are shown in Fig. 12(b) and (c). Furthermore, the mutual inductances between fifth coil and second, fourth, and sixth coils computed in both scenarios are shown in Fig. 12(d). In Fig. 12(b) and (d), the effect of ground plane on the quantities of interest is apparent. For the analysis at 2.5 GHz, the current distributions on the structure obtained in both scenarios are shown [Fig. 12(e) and (f)]. In the same analysis, the detailed breakdown of the memory usage and wall time is provided in Table I. Apparently, wall time for MVM involving sparse preconditioner $\overline{\mathbf{P}}$ is nearly the same as that for MVM involving MoM matrix $\overline{\mathbf{Z}}$ in both scenarios.

2) RF Coil Array: A 2-by-2 array of RF coils with center-to-center spacing 50 μm is analyzed by VoxHenry [Fig. 13(a)]. Each square RF coil with maximum length 40 μm is formed by conductors with square cross section 3×3 μm; its arm parallel to x-axis and below $z = 0$ is formed by two conductors with length 7 μm and a port is defined in the spacing between these conductors for each coil. The coils are excited (one at a time) at frequencies ranging from 1 Hz to 10 GHz (four equally spaced frequency points at each decade). Again, two different scenarios are considered. In the first scenario, the RF coil array is discretized by voxels of size 0.25 μm ($N = 4\,089\,600$ and $M = 2\,590\,656$). In the second scenario, a square ground plane with dimensions $110 \times 110 \times 2$ μm (width $\times$ length $\times$ height) is placed 2 μm below the bottom of coils and whole structure is discretized by voxels of size 0.25 μm ($N = 11\,833\,600$ and $M = 7\,437\,696$).

The frequency-dependent self-resistance and inductance of the first RF coil [i.e., the coil on the left bottom of the array in Fig. 13(a)] as well as the mutual inductances between the first RF coil and the remaining RF coils in the array obtained in both scenarios are shown in Fig. 13(b)–(d). The effect of ground plane on the quantities of interest is clearly

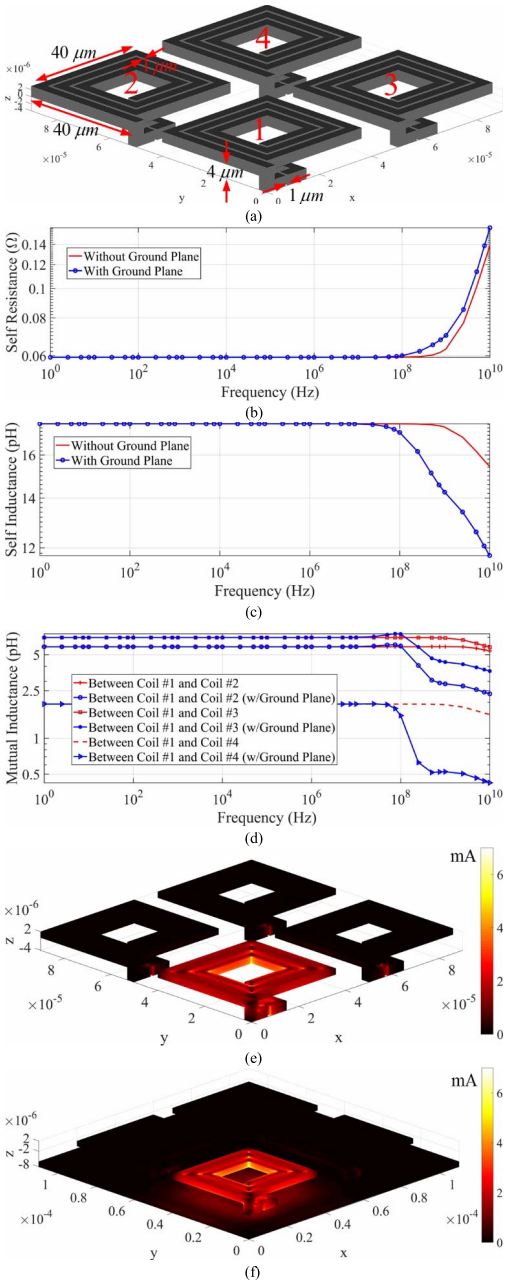

Fig. 13. (a) Geometry of RF coil array. The frequency-dependent (b) self-resistance and (c) self-inductance of the first RF coil. (d) Frequency-dependent mutual inductances of first RF coil with remaining coils when the ground plane does not exist and exists. The current distribution on the structure excited from the first port at 2.5 GHz when the ground plane (e) does not exist and (f) exists.

seen in the figures. Furthermore, the current distributions on the structure obtained in both scenarios are plotted for the analysis at 2.5 GHz [Fig. 13(e) and (f)]. For the same analysis, the detailed breakdown of the memory usage and wall time is given in Table II. In the first scenario, wall time for MVM involving $\overline{\mathbf{P}}$ is the half of that for MVM involving $\overline{\mathbf{Z}}$. In the second scenario, it is comparable with that for MVM involving $\overline{\mathbf{Z}}$.

V. CONCLUSION

VoxHenry, an FFT-accelerated inductance extractor, was presented for computing frequency-dependent inductances and

TABLE II
DETAILED BREAKDOWN OF THE MEMORY USAGE AND WALL TIME FOR THE RF COIL ARRAY EXAMPLE. UNITS FOR MEMORY AND WALL TIME ARE GB AND S.

	RF Coil Array	RF Coil Array with Ground Plane
N	4,089,600	11,833,600
M	2,590,656	7,437,696
K_t	3,628,800	8,518,400
Memory for $\overline{\mathbf{A}}_R$	0.23	0.67
Memory for $\mathcal{C}^{\beta,\alpha}$	4.43	10.49
Memory for LDLT decomposition of $\overline{\mathbf{S}}$	4.60	30.17
Number of iterations for solution of port #1 (tolerance=1e-8)	13	31
Time for filling out matrices & tensors	185.9	355.25
Time for iterative solution for all 4 ports	487.38	3714.09
Time for LDLT decomposition of $\overline{\mathbf{S}}$	17.55	70.41
Time for one MVM involving $\overline{\mathbf{Z}}$	5.19	12.17
Time for one MVM involving $\overline{\mathbf{P}}$	2.46	10.73
Time for one MVM involving $\overline{\mathbf{A}}_R$ and $\overline{\mathbf{A}}_R^T$	0.24	0.86

resistances of the structures discretized by voxels. VoxHenry solves the electric volume integral and current conservation equations after discretizing the currents on structures by a carefully selected basis function set, which allows accurately modeling the currents on arbitrarily shaped voxelized structures. During the iterative solution of such equations, VoxHenry leverages FFTs to accelerate MVMs and a sparse preconditioner to ensure the rapid convergence of iterative solution. Numerical results showed the applicability, accuracy, and efficiency of the proposed VoxHenry inductance extractor. In specific, VoxHenry computed the frequency-dependent inductance of a circular coil with three digit accuracy, showing its accuracy for arbitrarily shaped voxelized structures. Furthermore, VoxHenry completed the simulation of an RF coil array with ground plane for one frequency point in 62 min, which involve the solution of a linear system of equations with 19 271 296 unknowns; this demonstrates the efficiency of the proposed VoxHenry-inductance extractor.

APPENDIX A
ENTRIES OF $\overline{\mathbf{Z}}$, $\overline{\mathbf{A}}^T$, AND $\mathbf{I}$

Assume that the basis functions $\mathbf{f}_k^x(\mathbf{r})$, $\mathbf{f}_k^y(\mathbf{r})$, $\mathbf{f}_k^z(\mathbf{r})$, $\mathbf{f}_k^{2D}(\mathbf{r})$, $\mathbf{f}_k^{3D}(\mathbf{r})$ are numbered between 1 and K, $K+1$ and $2K$, $2K+1$ and $3K$, $3K+1$ and $4K$, and $4K+1$ and $5K$, respectively. Then, the entries of unknown current coefficient vector $\mathbf{I}I_k$, $k=1,\ldots,5K$, $(N=5K)$ are

$$I_k = \begin{cases} I_k^x, & 1 \le k \le K \\ I_k^y, & K+1 \le k \le 2K \\ I_k^z, & 2K+1 \le k \le 3K \\ I_k^{2D}, & 3K+1 \le k \le 4K \\ I_k^{3D}, & 4K+1 \le k \le 5K. \end{cases} \tag{19}$$

To obtain the linear system of equations in (9), first the current density $\mathbf{J}(\mathbf{r})$ in (1) is expanded in terms of basis functions $\mathbf{f}_k^\alpha(\mathbf{r})$, then the resulting equation is tested with $\mathbf{f}_l^\beta(\mathbf{r})$, where $\alpha,\beta \in \{x,y,z,2D,3D\}$. The resulting entries of the blocks in $\overline{\mathbf{Z}}$ and $\overline{\mathbf{Z}}^{\beta,\alpha}$, are

$$\overline{\mathbf{Z}}_{lk}^{x,x} = \frac{\delta_{lk}}{\sigma\,\Delta x} - w\int_{V_l}\int_{V_k'} G(\mathbf{r},\mathbf{r}')dV'dV \tag{20}$$

$$\overline{\mathbf{Z}}_{lk}^{2D,2D} = \frac{\delta_{lk}}{\sigma(6\Delta x)} - \frac{w}{(\Delta x)^2}\left(\int_{V_l}(x-x_l)\int_{V_k'}(x'-x_k)G(\mathbf{r},\mathbf{r}')dV'dV + \int_{V_l}(y-y_l)\int_{V_k'}(y'-y_k)G(\mathbf{r},\mathbf{r}')dV'dV\right) \tag{21}$$

$$\overline{\mathbf{Z}}_{lk}^{3D,3D} = \frac{\delta_{lk}}{\sigma(2\Delta x)} - \frac{w}{(\Delta x)^2}\left(\int_{V_l}(x-x_l)\int_{V_k'}(x'-x_k)G(\mathbf{r},\mathbf{r}')dV'dV + \int_{V_l}(y-y_l)\int_{V_k'}(y'-y_k)G(\mathbf{r},\mathbf{r}')dV'dV + 4\int_{V_l}(z-z_l)\int_{V_k'}(z'-z_k)G(\mathbf{r},\mathbf{r}')dV'dV\right) \tag{22}$$

$$\overline{\mathbf{Z}}_{lk}^{x,2D} = -\frac{w}{\Delta x}\int_{V_l}\int_{V_k'}(x'-x_k)G(\mathbf{r},\mathbf{r}')dV'dV \tag{23}$$

$$\overline{\mathbf{Z}}_{lk}^{y,2D} = \frac{w}{\Delta x}\int_{V_l}\int_{V_k'}(y'-y_k)G(\mathbf{r},\mathbf{r}')dV'dV \tag{24}$$

$$\overline{\mathbf{Z}}_{lk}^{z,3D} = \frac{2w}{\Delta x}\int_{V_l}\int_{V_k'}(z'-z_k)G(\mathbf{r},\mathbf{r}')dV'dV \tag{25}$$

$$\overline{\mathbf{Z}}_{lk}^{2D,3D} = \frac{w}{(\Delta x)^2}\left(\int_{V_l}(x-x_l)\int_{V_k'}(x'-x_k)G(\mathbf{r},\mathbf{r}')dV'dV - \int_{V_l}(y-y_l)\int_{V_k'}(y'-y_k)G(\mathbf{r},\mathbf{r}')dV'dV\right) \tag{26}$$

where $w = j\omega\mu/(\Delta x)^4$, $\delta_{lk}=1$ for $l=k$, otherwise $\delta_{lk}=0$. We should note here that some blocks can be obtained from the transpose of other blocks: $\overline{\mathbf{Z}}^{2D,x} = (\overline{\mathbf{Z}}^{x,2D})^T$, $\overline{\mathbf{Z}}^{2D,y} = (\overline{\mathbf{Z}}^{y,2D})^T$, and $\overline{\mathbf{Z}}^{3D,z} = (\overline{\mathbf{Z}}^{z,3D})^T$. Furthermore, many blocks are the same: $\overline{\mathbf{Z}}^{x,x} = \overline{\mathbf{Z}}^{y,y} = \overline{\mathbf{Z}}^{z,z}$, $\overline{\mathbf{Z}}^{x,2D} = \overline{\mathbf{Z}}^{x,3D}$, $\overline{\mathbf{Z}}^{y,2D} = -\overline{\mathbf{Z}}^{y,3D}$, $\overline{\mathbf{Z}}^{2D,x} = \overline{\mathbf{Z}}^{3D,x}$, $\overline{\mathbf{Z}}^{2D,y} = -\overline{\mathbf{Z}}^{3D,y}$, and $\overline{\mathbf{Z}}^{3D,2D} = \overline{\mathbf{Z}}^{2D,3D}$. The integrals in (20)–(26) are evaluated using the methods described in [21]–[23].

The entries of $\overline{\mathbf{A}}^T$ are obtained by testing $\nabla\Phi(\mathbf{r})$ with $\mathbf{f}_l^\beta(\mathbf{r})$, $\beta \in \{x,y,z,2D,3D\}$. Consider the volume integral resulting from this testing operation

$$\left\langle \frac{\mathbf{f}_l^\beta(\mathbf{r})}{\Delta x^2}, \nabla\Phi(\mathbf{r}) \right\rangle = \frac{1}{\Delta x^2}\int_{V_l}\mathbf{f}_l^\beta(\mathbf{r})\cdot\nabla\Phi(\mathbf{r})dV. \tag{27}$$

TABLE III
SIGNS OF BLOCK TOEPLITZ TENSOR FOR CONSTRUCTING EACH BLOCK IN EACH CIRCULANT TENSOR

Block / Toeplitz tensor	L	M	N	LM	LN	MN	LMN
$\mathcal{G}^{x,x}$	+	+	+	+	+	+	+
$\mathcal{G}^{2D,2D}$	+	+	+	+	+	+	+
$\mathcal{G}^{3D,3D}$	+	+	+	+	+	+	+
$\mathcal{G}^{x,2D}$	-	+	+	-	-	+	-
$\mathcal{G}^{y,2D}$	+	-	+	-	+	-	-
$\mathcal{G}^{2D,x}$	-	+	+	-	-	+	-
$\mathcal{G}^{2D,y}$	+	-	+	-	+	-	-
$\mathcal{G}^{z,3D}$	+	+	-	+	-	-	-
$\mathcal{G}^{3D,z}$	+	+	-	+	-	-	-
$\mathcal{G}^{2D,3D}$	+	+	+	+	+	+	+

Applying the divergence theorem and invoking the divergence-free property of $\mathbf{f}_l^\beta(\mathbf{r})$ yields

$$\left\langle \frac{\mathbf{f}_l^\beta(\mathbf{r})}{\Delta x^2}, \nabla\Phi(\mathbf{r}) \right\rangle = \frac{1}{\Delta x^2} \sum_{i=1}^{6} \int_{S_{l,i}} \Phi(\mathbf{r}) \mathbf{f}_l^\beta(\mathbf{r}) \cdot \hat{\mathbf{n}}_{l,i}\, dS \quad (28)$$

where $S_{l,i}$ is the ith surface of V_l with outward pointing unit normal $\hat{\mathbf{n}}_{l,i}$ and houses mth node, $m \in \{1, \ldots, M\}$. Evaluation of each surface integral (with nonzero integrand) yields the value of $\Phi(\mathbf{r})$ on mth node and a constant. While the former is the mth entry of $\mathbf{\Phi}$, the latter is an entry of $\overline{\mathbf{A}}^T$ as

$$\overline{\mathbf{A}}^T_{lm} = \begin{cases} \pm 1, & \beta = x \text{ and } \hat{\mathbf{n}}_{l,i} = \pm\hat{\mathbf{x}} \\ \pm 1, & \beta = y \text{ and } \hat{\mathbf{n}}_{l,i} = \pm\hat{\mathbf{y}} \\ \pm 1, & \beta = z \text{ and } \hat{\mathbf{n}}_{l,i} = \pm\hat{\mathbf{z}} \\ \{0.5, -0.5\}, & \beta = 2D \text{ and } \hat{\mathbf{n}}_{l,i} = \{\pm\hat{\mathbf{x}}, \pm\hat{\mathbf{y}}\} \\ \{0.5, 0.5, -1\}, & \beta = 3D \text{ and } \hat{\mathbf{n}}_{l,i} = \{\pm\hat{\mathbf{x}}, \pm\hat{\mathbf{y}}, \pm\hat{\mathbf{z}}\}. \end{cases} \quad (29)$$

APPENDIX B
BLOCK TOEPLITZ AND CIRCULANT TENSORS

To obtain a block Toeplitz tensor $\mathcal{G}^{\beta,\alpha}$ corresponding a block $\overline{\mathbf{Z}}^{\beta,\alpha}$ in (10), the voxels (empty and nonempty ones) are numbered with indices $\mathbf{k} = (k_x, k_y, k_z)$, $k_x = 1, \ldots, K_x$, $k_y = 1, \ldots, K_y$, and $k_z = 1, \ldots, K_z$. Then, the basis function in the first voxel with the indices $(1, 1, 1)$ is assigned as the basis function. Finally, the entries of the Toeplitz tensor $\mathcal{G}^{\beta,\alpha}_{k_x,k_y,k_z}$ is obtained by sweeping over all testing functions on all voxels with the indices (k_x, k_y, k_z), $k_x = 1, \ldots, K_x$, $k_y = 1, \ldots, K_y$, and $k_z = 1, \ldots, K_z$, and evaluating the corresponding integral in (20)–(26). [Note that $\delta_{lk} = 0$ in (20)–(22) for $(k_x, k_y, k_z) = (1, 1, 1)$.] For example, the entries of $\mathcal{G}^{x,x}$ corresponding to the block $\overline{\mathbf{Z}}^{x,x}$ are obtained by evaluating (20) after setting $\delta_{lk} = 0$.

A block circulant tensor $\mathcal{C}^{\beta,\alpha}$ corresponding to a block in $\overline{\mathbf{Z}}^{\beta,\alpha}$ in (10) is obtained by properly embedding the related block Toeplitz tensor $\mathcal{G}^{\beta,\alpha}$ in $\mathcal{C}^{\beta,\alpha}$. To this end, the procedure explained in Appendix B of [3] is followed. The signs of the Toeplitz blocks used to construct the blocks of circulant tensor are assigned as in Table III. Note that this table corresponds to of [3, Table V] and the blocks in circulant tensor are labeled by L, M, N, LM, LN, MN, and LMN, as in [3].

REFERENCES

[1] K. Gala, V. Zolotov, R. Panda, B. Young, J. Wang, and D. Blaauw, "On-chip inductance modeling and analysis," in *Proc. 37th Annu. Design Autom. Conf.*, Los Angeles, CA, USA, 2000, pp. 63–68.

[2] M. Fujishima and S. Amakawa, "Recent progress and prospects of terahertz CMOS," *IEICE Electron. Exp.*, vol. 12, no. 13, pp. 1–7, 2015.

[3] A. G. Polimeridis, J. F. Villena, L. Daniel, and J. K. White, "Stable FFT-JVIE solvers for fast analysis of highly inhomogeneous dielectric objects," *J. Comput. Phys.*, vol. 269, pp. 280–296, Jul. 2014.

[4] M. F. Catedra, E. Gago, and L. Nuno, "A numerical scheme to obtain the RCS of three-dimensional bodies of resonant size using the conjugate gradient method and the fast Fourier transform," *IEEE Trans. Antennas Propag.*, vol. 37, no. 5, pp. 528–537, May 1989.

[5] H. Gan and W. C. Chew, "A discrete BCG-FFT algorithm for solving 3D inhomogeneous scatterer problems," *J. Electromagn. Waves Appl.*, vol. 9, pp. 1339–1357, Apr. 1995.

[6] J. R. Phillips and J. K. White, "A precorrected-FFT method for electrostatic analysis of complicated 3-D structures," *IEEE Trans. Comput.-Aided Design Integr. Circuits Syst.*, vol. 16, no. 10, pp. 1059–1072, Oct. 1997.

[7] E. Bleszynski, M. Bleszynski, and T. Jaroszewic, "AIM: Adaptive integral method for solving large-scale electromagnetic scattering and radiation problems," *Radio Sci.*, vol. 31, no. 5, pp. 1225–1251, Sep./Oct. 1996.

[8] R. L. Wagner, J. Song, and W. C. Chew, "Monte Carlo simulation of electromagnetic scattering from two-dimensional random rough surfaces," *IEEE Trans. Antennas Propag.*, vol. 45, no. 2, pp. 235–245, Feb. 1997.

[9] M. Kamon, M. J. Tsuk, and J. K. White, "FASTHENRY: A multipole-accelerated 3-D inductance extraction program," *IEEE Trans. Microw. Theory Techn.*, vol. 42, no. 9, pp. 1750–1758, Sep. 1994.

[10] A. C. Yucel, I. P. Georgakis, A. G. Polimeridis, H. Bagci, and J. K. White, "VoxHenry: FFT-accelerated inductance extraction for voxelized geometries," in *Proc. 38th Prog. Electromagn. Res. Symp.*, Saint Petersburg, Russia, May 2017, p. 91.

[11] A. E. Ruehli, "Survey of computer-aided electrical analysis of integrated circuit interconnections," *IBM J. Res. Develop.*, vol. 23, no. 6, pp. 626–639, 1979.

[12] A. C. Cangellaris, J. Prince, and L. P. Vakanas, "Frequency-dependent inductance and resistance calculation for three-dimensional structures in high-speed interconnect systems," *IEEE Trans. Compon., Hybrids, Manuf. Technol.*, vol. 13, no. 1, pp. 154–159, Mar. 1990.

[13] C.-T. Tsai, H. Massoudi, C. H. Durney, and M. F. Iskander, "A procedure for calculating fields inside arbitrarily shaped, inhomogeneous dielectric bodies using linear basis functions with the moment method," *IEEE Trans. Microw. Theory Techn.*, vol. MTT-34, no. 11, pp. 1131–1139, Nov. 1986.

[14] W. T. Weeks, L. L.-H. Wu, M. F. McAllister, and A. Singh, "Resistive and inductive skin effect in rectangular conductors," *IBM J. Res. Develop.*, vol. 23, no. 6, pp. 652–660, 1979.

[15] B. Krauter and L. T. Pileggi, "Generating sparse partial inductance matrices with guaranteed stability," in *Proc. IEEE/ACM Int. Conf. CAD*, San Jose, CA, USA, Nov. 1995, pp. 45–52.

[16] R. A. Horn and F. Zhang, "Basic properties of the schur complement," in *The Schur Complement and Its Applications*. Boston, MA, USA: Springer, 2005, pp. 17–46.

[17] T. A. Davis, *Direct Methods for Sparse Linear Systems*. Philadelphia, PA, USA: SIAM, 2006.

[18] *Radio Instruments and Measurements—Circular C74*, Washington, DC, USA, U.S. Government Printing Office, 1924.

[19] S. C. Thierauf, *High-Speed Circuit Board Signal Integrity*. Norwood, MA, USA: Artech House, 2004.

[20] L. Daniel, A. Sangiovanni-Vincentelli, and J. White, "Proximity templates for modeling of skin and proximity effects on packages and high frequency interconnect," in *Proc. IEEE/ACM Int. Conf. CAD*, San Jose, CA, USA, Nov. 2002, pp. 326–333.

[21] A. G. Polimeridis, F. Vipiana, J. R. Mosig, and D. R. Wilton, "DIRECTFN: Fully numerical algorithms for high precision computation of singular integrals in Galerkin SIE methods," *IEEE Trans. Antennas Propag.*, vol. 61, no. 6, pp. 3112–3122, Jun. 2013.

[22] A. G. Polimeridis, J. F. Villena, L. Daniel, and J. K. White, "Robust J-EFVIE solvers based on purely surface integrals," in *Proc. Int. Conf. Electromagn. Adv. Appl. (ICEAA)*, Turin, Italy, 2013, pp. 379–381.
[23] I. P. Georgakis and A. G. Polimeridis, "Reduction of volume-volume integrals arising in Galerkin JM-VIE formulations to surface-surface integrals," in *Proc. Eur. Conf. Antennas Propag. (EuCAP)*, Paris, France, 2017, pp. 324–326.

Abdulkadir C. Yucel received the B.S. degree (*summa cum laude*) in electronics engineering from the Gebze Institute of Technology, Kocaeli, Turkey, in 2005, and the M.S. and Ph.D. degrees in electrical engineering from the University of Michigan, Ann Arbor, MI, USA, in 2008 and 2013, respectively.

From 2005 to 2006, he was a Research and Teaching Assistant at the Electronics Engineering Department, Gebze Institute of Technology. From 2006 to 2013, he was a Graduate Student Research Assistant with the Radiation Laboratory, University of Michigan, where he was a Research Fellow from 2013 to 2015. Since 2016, he has been a Post-Doctoral Researcher with the Research Laboratory of Electronics, Massachusetts Institute of Technology, Cambridge, MA, USA, and affiliated with the Computational Electromagnetics Group, King Abdullah University of Science and Technology, Thuwal, Saudi Arabia. His current research interests include computational electromagnetics with emphasis on uncertainty quantification for electromagnetic analysis on complex platforms, electromagnetic compatibility and interference analysis, nature-based design of electromagnetic devices, integral equation-based frequency, and time-domain solvers and their accelerators.

Dr. Yucel was a recipient of the Fulbright Fellowship in 2006, the Electrical Engineering and Computer Science Departmental Fellowship of the University of Michigan in 2007, and the Student Paper Competition Honorable Mention Award of the IEEE International Symposium on Antennas and Propagation Symposium in 2009. He has been serving as an Associate Editor for the *International Journal of Numerical Modelling: Electronic Networks, Devices, and Fields* and as a Reviewer for various technical journals.

Ioannis P. Georgakis received the Diploma degree in electrical engineering and computer science from the Aristotle University of Thessaloniki, Thessaloniki, Greece, in 2014. He is currently pursuing the Ph.D. degree at the Center for Computational Data-Intensive Science and Engineering, Skolkovo Institute of Science and Technology, Moscow, Russia.

His current research interests include computational electromagnetics, with an emphasis in volume integral equation methods for magnetic resonance imaging modeling.

Mr. Georgakis was a recipient of three scholarships of academic excellence by the State Scholarship Foundation during his undergraduate studies (2010–2012).

Athanasios G. Polimeridis (SM'16) was born in Thessaloniki, Greece, in 1980. He received the Diploma and Ph.D. degrees in electrical engineering and computer science from the Aristotle University of Thessaloniki, Thessaloniki, in 2003 and 2008, respectively.

From 2008 to 2012, he was a Post-Doctoral Research Associate with the Laboratory of Electromagnetics and Acoustics, École Polytechnique Fédérale de Lausanne, Lausanne, Switzerland. From 2012 to 2015, he was a Post-Doctoral Research Associate with the Massachusetts Institute of Technology, Cambridge, MA, USA, where he was a member of the Computational Prototyping Group, Research Laboratory of Electronics. He is currently an Assistant Professor with the Skolkovo Institute of Science and Technology, Moscow, Russia. His current research interests include computational methods for problems in physics and engineering (classical electromagnetics, quantum and thermal electromagnetic interactions, and magnetic resonance imaging) with an emphasis on the development and implementation of integral-equation-based algorithms.

Dr. Polimeridis was a recipient of the Swiss National Science Foundation Fellowship for Advanced Researchers in 2012.

Hakan Bağcı (S'98–M'07–SM'14) received the B.S. degree in electrical and electronics engineering from Bilkent University, Ankara, Turkey, in 2001, and the M.S. and Ph.D. degrees in electrical and computer engineering from the University of Illinois at Urbana–Champaign (UIUC), Urbana, IL, USA, in 2003 and 2007, respectively.

From 1999 to 2001, he was an Undergraduate Researcher with the Computational Electromagnetics Group, Bilkent University. From 2001 to 2006, he was a Research Assistant with the Center for Computational Electromagnetics and Electromagnetics Laboratory, UIUC. From 2007 to 2009, he was a Research Fellow with the Radiation Laboratory, University of Michigan, Ann Arbor, MI, USA. In 2009, he joined the Division of Physical Sciences and Engineering, King Abdullah University of Science and Technology, Thuwal, Saudi Arabia, as an Assistant Professor of electrical engineering. He has authored or co-authored nine finalist papers of the Student Paper Competition of the 2005, 2008, 2010, and 2014 IEEE Antennas and Propagation Society International Symposiums and 2013 and 2014 Applied Computational Electromagnetics Society Conferences. His current research interests include computational electromagnetics with emphasis on time-domain integral equations and their fast marching-on-in-time-based solutions, well-conditioned integral-equation formulations, and the development of fast hybrid methods for analyzing statistical electromagnetic compatibility/electromagnetic interference phenomena on complex and fully loaded platforms.

Dr. Bağcı was a recipient of the 2008 International Union of Radio Scientists Young Scientist Award and the 2004–2005 Interdisciplinary Graduate Fellowship of the Computational Science and Engineering Department, UIUC. His paper "Fast and Rigorous Analysis of EMC/EMI Phenomena on Electrically Large and Complex Structures Loaded with Coaxial Cables" was one of the three finalists (with honorable mention) of the 2008 Richard B. Schulz Best Transactions Paper Award given by the IEEE Electromagnetic Compatibility Society.

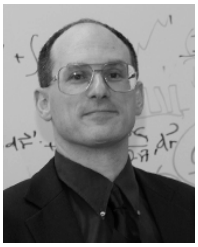

Jacob K. White (F'08) received the B.S. degree in electrical engineering and computer science (EECS) from the Massachusetts Institute of Technology (MIT), Cambridge, MA, USA, in 1980, and the S.M. and Ph.D. degrees in EECS from the University of California at Berkeley, Berkeley, CA, USA, in 1983 and 1985, respectively.

He was with the IBM T. J. Watson Research Center. He joined EECS, MIT, as an Analog Devices Career Development Assistant Professor in 1987. He is currently the C. H. Green Professor with the EECS Department, MIT, where he is involved in simulation and optimization techniques for problems in medical technology, nanophotonics, and electrical circuits and interconnect; and experimenting with blended computation- and maker-centric strategies for teaching control, machine learning, and electromagnetics.

Dr. White was a co-recipient of the 2013 A. R. Newton Technical Impact Award in EDA with Keith Nabors for their fast capacitance extraction program FastCap. He was a Presidential Young Investigator in 1988, an Associate Editor of the IEEE TRANSACTIONS ON COMPUTER-AIDED DESIGN OF INTEGRATED CIRCUITS AND SYSTEMS from 1992 to 1996, a member of the Spectre/SpectreRF development team from 1989 to 1999, a Chair of the International Conference on Computer-Aided Design in 1999, served as an Associate Director of the Research Laboratory of Electronics, MIT, from 2001 to 2006, an Academic Research Fellow of Ansoft/Ansys from 2010 to 2016, and served as the MIT EECS Co-Education Officer from 2011 to 2014.